Sustainable Marine Structures
https://journals.nasspublishing.com/index.php/sms

RESEARCH **ARTICLE**

Derivation of 3D Dynamics for Rigid Floating Structures under Directional Wave Excitation

Shengzhe Wang

Department of Civil Engineering, University of Colorado Denver, Denver, CO 80204, USA

ABSTRACT

Modular floating structures (MFS) offer a sustainable pathway towards the expansion of coastal cities in adaptation to flooding and sea level rise driven by climate change. It is therefore necessary to develop analytical methods easily accessible to architects or structural engineers for the rapid prototyping of MFS designs. This work develops novel closed-form expressions describing the rigid body dynamics of symmetrically loaded rectangular pontoons across all six degrees of freedom (DOF) excited by surface waves approaching from any arbitrary direction. The derivations were based on Airy wave theory assuming frequency-independent added mass and damping. When benchmarked against numerical solutions from ANSYS/AQWA for two MFS prototypes, the analytical approach proved capable of predicting the response amplitude operators (RAO) across all DOFs, wave directions, and structural configurations. However, while the response of mass-dominated DOFs (surge, sway, and yaw) were well captured, the damping ratio for stiffness-dominated DOFs (heave, roll, and pitch) must be judiciously selected to yield accurate RAO results. A parametric investigation further elucidated the contribution of structural geometry and wave directionality on the critical accelerations experienced by an idealized floating structure founded upon a square pontoon under realistic sea states. It was discovered that the largest accelerations were triggered by waves approaching orthogonally to the pontoon. Ultimately, this work facilitates a more streamlined approach for the dynamic analysis of compliant floating bodies to supplement detailed modeling efforts via numerical methods.

Keywords: Floating Structure; Airy Waves; Pontoon; RAO; Damping; Climate Adaptation

*CORRESPONDING AUTHOR:
Shengzhe Wang, Department of Civil Engineering, University of Colorado Denver, Denver, CO 80204, USA;
Email: shengzhe.2.wang@ucdenver.edu

ARTICLE INFO
Received: 18 December 2024 | Revised: 29 December 2024 | Accepted: 5 February 2025 | Published Online: 6 March 2025
DOI: https://doi.org/10.36956/sms.v7i1.1545

CITATION
Wang, S., 2025. Derivation of 3D Dynamics for Rigid Floating Structures under Directional Wave Excitation. Sustainable Marine Structures. 7(1): 35–51. DOI: https://doi.org/10.36956/sms.v7i1.1545

1. Introduction

Coastal areas often exhibit high population densities and are home to the majority of the world's megacities [1, 2]. As an example, land within 100 km of the ocean supports 40% of the earth's inhabitants and hosts 60% of all "Alpha" level cities classified by the Globalization and World Cities (GaWC) Research Network (**Figure 1**) [3, 4]. Yet, continued migration and urbanization have placed increasing strain on nearshore metropolises such that by 2060, it is predicted that up to 1.4 billion people may reside in low-elevation coastal zones (LECZ) below 10 m in elevation [5]. With accelerating climate change and sea level rise, the inhabitants of LECZs will be highly susceptible to extreme flooding and land loss approaching 1.79 million km2 by the 22nd century [6, 7]. In response, the United Nations Human Settlements Program (UN-Habitat) launched its inaugural Round Table on Sustainable Floating Cities (in collaboration with OCEANIX and the Massachusetts Institute of Technology) in April 2019 to spearhead the development of floating cities for ocean colonization [8]. This was quickly followed by the "Future World Vision" initiative launched by the American Society of Civil Engineers (ASCE) to explore the idea of sustainable floating infrastructure solutions for climate resilience and adaptation [9].

Floating settlements typically comprise a collection of individual pontoons (commonly referred to as "modules") judicially arranged to give rise to a symbiotic community (see **Figure 1**). Unlike traditional land reclamation which becomes economically prohibitive at depths greater than 20 m [10], modular floating structures (MFS) are not limited by water depth or seabed conditions. Floating structures also avoid the need for soil consolidation thus translating to much faster construction times while enabling immediate occupancy relative to reclaimed land. Their modular nature further promotes easy expansion and relocation based on societal needs with minimal impact on the seabed ecosystem and can also foster new habitats to support a range of aquatic life [11]. Being inherently base-isolated, floating structures are especially resilient to seismic events as evidenced by the Kansai International Airport floating terminal which suffered no damage during the Great Hanshin Earthquake of 1995 [12]. In addition to the aforementioned advantages, MFS are immune to future sea level rise and coastal flooding thus exemplifying a "no-regret" strategy towards climate adaptation.

Figure 1. Location of Alpha-category coastal cities and examples of floating settlements including: (**a**) Floating homes in Seattle [13]; (**b**) Floating village on Lake Titicaca, Peru [14]; (**c**) Schoonschip floating district, Amsterdam (https://schoonschipamsterdam.org); (**d**) Floating city proposal for Busan, South Korea (OCEANIX/BIG-Bjarke Ingels Group); (**e**) Kenzo Tange's 1960 plan for Tokyo Bay [15].

Despite the surplus of benefits offered by pontoon-supported floating structures, little technical guidance is available to the structural engineering and architectural community pertaining to their design. A crucial element of this design process involves ascertaining the dynamic response about all six degrees of freedom mobilized by waves approaching from any arbitrary direction. This phenomenon is highly complex and is dependent upon the MFS geometry and characteristics of incident waves. Hence, numerical methods are commonly employed for the hydrodynamic analysis of floating structures. Examples include the ANSYS/AQWA [16] and HYDROSTAR [17] solvers based on potential theory. Gutierrez-Romero et al. [18] also employed nonlinear finite element methods (FEM) to compute the dynamics of floating offshore wind turbines, whereas Rahman et al. [19] adopted the volume of fluid (VOF) technique to simulate a floating breakwater. Finally, mesh-free Lagrangian methods such as smoothed particle hydrodynamics (SPH) have recently attained popularity for the modeling of floating systems [20, 21].

While numerical methods of analysis remain widely popular within marine and offshore industries, the design of floating structures for human habitation must receive input from architects and structural engineers familiar with traditional land-based buildings. Such groups are unlikely to be accustomed to compu-

tational fluid dynamics (CFD) thus necessitating the derivation of simplified analytical methods for the dynamic analysis of floating pontoons [22]. This is especially true during the preliminary design phase where prospective solutions within a vast parametric design space must be rapidly assessed and calibrated or discarded as a precursor to in-depth CFD modeling. In this regard, analytical solutions have only been proposed for orthogonal waves (i.e., purely longitudinal or transverse) in the context of rectangular pontoons, which severely limits their overall usefulness [23, 24]. It is therefore necessary to develop more general expressions describing the dynamic response of an MFS that enables the coupling between all six of its DOFs applicable to oblique waves.

This paper formulates generalized solutions to describe waves interacting with a symmetrically loaded rectangular pontoon approaching from any arbitrary direction. Simplified closed-form expressions were derived based on Airy wave theory and frequency-independent added mass and damping to capture both Froude-Krylov and diffraction/radiation forces. The expressions enable the response pertaining to all six DOFs (surge, sway, heave, roll, pitch, and yaw) of an MFS to be rapidly determined for oblique surface waves propagating in deep or depth-limited waters. The solutions were subsequently validated against numerical simulations performed using the commercial ANSYS/AQWA potential theory solver. A parametric study was finally employed to elucidate the role of superstructure geometry on the dynamic response of a floating structure within realistic sea states as a function of wave directionality. Ultimately, this work provides architects and structural engineers with an accurate yet accessible approach to obtaining the 3D translational and rotational rigid body dynamics of idealized floating bodies under arbitrary wave conditions. It is hoped that the resulting framework will help foster the widespread adoption of modular floating structures as a sustainable form of land creation for ocean colonization and climate adaptation.

2. Theoretical Background

The dynamic response of floating structures under wave excitation can be broadly classified into hydroelastic or rigid body regimes based on the transitional length. When approximating the structure as a beam with uniform stiffness, the transitional length suggested by Suzuki and Yoshida [25] is:

$$L_c = 2\pi \left(\frac{E_b I_b}{k_c} \right)^{1/4} \tag{1}$$

where $E_b I_b$ is the elastic bending stiffness and k_c denotes the heave stiffness of the hydrostatic restoring force per unit length. Large floating structures such as VLFS mats with lengths longer than L_c are governed by hydroelastic behavior (i.e., elastic deformations of the pontoon) whereas an MFS shorter than L_c can be treated as a rigid body. The dynamic response of a rigid body in waves can be determined based on the response amplitude operator (RAO), defined as the response amplitude (R_0) per unit wave amplitude (A), associated with each of its six degrees of freedom (DOF):

$$\text{RAO}_R = \frac{R_0}{A} \tag{2}$$

where:

$$R = \begin{cases} x, \text{Surge} \\ y, \text{Sway} \\ z, \text{Heave} \\ \theta_x, \text{Roll} \\ \theta_y, \text{Pitch} \\ \theta_z, \text{Yaw} \end{cases}, \quad R_0 = \begin{cases} x_0, \text{Surge amplitude} \\ y_0, \text{Sway amplitude} \\ z_0, \text{Heave amplitude} \\ \theta_{x0}, \text{Roll amplitude} \\ \theta_{y0}, \text{Pitch amplitude} \\ \theta_{z0}, \text{Yaw amplitude} \end{cases} \tag{3}$$

Here, R denotes the time-varying response pertaining to a given DOF whereas R_0 is the amplitude of the response. Knowledge of R_0 therefore enables the time-varying translation/rotation (R) to be determined via:

$$R(t) = R_0 cos(\omega t - \varphi_R) \tag{4}$$

where $\omega = 2\pi f$ is the wave frequency and φ_R is the phase lag. When assuming a compliantly moored MFS, the floating body can be idealized using vertical and rotational springs to represent the heave and roll/pitch stiffness, respectively, as shown in **Figure 2**. Since the frequency of wave excitation in surge, sway, and yaw is expected to be much greater than the corresponding natural frequency, their response will largely be governed by the body's inertia [24, 26]. As such, the RAOs about a

given DOF can be classified as either mass- or stiffness-dominated and expressed as:

$$\text{RAO}_R = \begin{cases} \frac{Q_R F_{0R}}{K_R}, \text{Stiffness-dominated (heave, roll, pitch)} \\ \frac{F_{0R}}{M_R \omega^2}, \text{Mass-dominated (sway, surge, yaw)} \end{cases} \tag{5}$$

where the subscript $R = \{x, y, z, \theta_x, \theta_y, \theta_z\}$ describes the corresponding DOF per Equation (3). Q_R is the frequency-dependent dynamic amplification factor:

$$Q_R = \frac{1}{\sqrt{\left(1 - \frac{f^2}{f_{nR}^2}\right)^2 + \left(2\xi_R \frac{f}{f_{nR}}\right)^2}} \tag{6}$$

with ξ_R being the damping ratio for DOF R and:

$$f_{nR} = \frac{1}{2\pi}\sqrt{\frac{K_R}{M_R}} \tag{7}$$

is the natural frequency associated with R for stiffness-dominated DOFs. K_R and M_R respectively signify the corresponding stiffness and total mass attributed to the dynamic response in R. Similar to the RAO, the phase lag ϕ_R is also treated differently for mass- and stiffness-dominated DOFs:

$$\phi_R = \begin{cases} \arctan\left(\frac{2\xi_R \frac{f}{f_{nR}}}{1 - \frac{f^2}{f_{nR}^2}}\right), \text{Stiffness-dominated (heave, roll, pitch)} \\ \pi, \text{Mass-dominated (sway, surge, yaw)} \end{cases} \tag{8}$$

Finally, the term F_{0R} in Equation (5) refers to the forcing amplitude accounting for both Froude-Krylov and added mass forces associated with R. Computing the RAO for any given DOF R therefore requires the determination of the associated stiffness (K_R), mass (M_R), and forcing amplitude (F_{0R}).

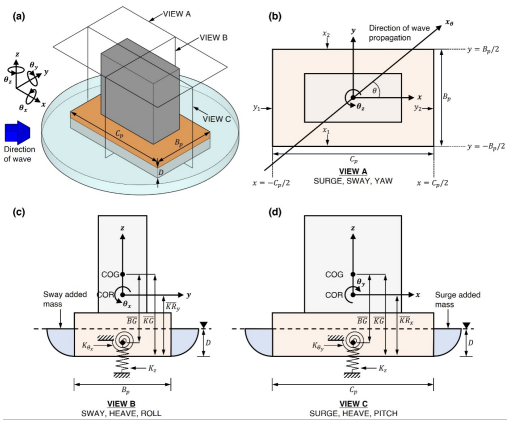

Figure 2. Geometric description of the idealized floating structure showing: (**a**) 3D; (**b**) Plan; (**c**) Front elevation; (**d**) Side elevation views.

2.1. Waterplane Stiffness

The waterplane stiffness for heave (z), roll (θ_x), and pitch (θ_y) DOFs are based on the hydrostatic stiffness shown as springs in **Figure 2** and given by:

$$K_R = \begin{cases} K_{\theta_x} = \rho g \left(I_x - \bar{BG}\, V\right), \text{Roll} \\ K_{\theta_y} = \rho g \left(I_y - \bar{BG}\, V\right), \text{Pitch} \\ K_z = \rho g B_p C_p, \text{Heave} \end{cases} \tag{9}$$

where $\bar{BG} = \bar{KG} - D/2$ is the vertical distance from the center of buoyancy (taken at half the draft D above the keel) to the center of gravity (COG) as shown in **Figure 2** and $V = C_p B_p D$ is the total submerged volume of a rectangular pontoon with length C_p and width B_p (**Figure 2**). From Archimedes' principle, the draft (submerged height) of an MFS with mass m_s in water of density ρ is:

$$D = \frac{m_s}{\rho B_p C_p} \tag{10}$$

while:

$$I_x = \frac{C_p B_p^3}{12} \quad , \quad I_y = \frac{B_p C_p^3}{12} \tag{11}$$

respectively denote the waterplane second moments of area about the x and y axis for a rectangular pontoon.

2.2. Hydrodynamic Mass

The total mass M_R mobilized for a given DOF R must account for both the structural mass (m_s) and hydrodynamic added mass (m_{aR}). The added mass accounts for wave diffraction around the floating body and is affected by its geometry, orientation, and oscillation frequency [26]. In this work, a simplified approach is adopted where the added mass is treated as a frequency-independent prismatic volume of water synchronized with the MFS response as shown in **Figure 3** [27]. To avoid the use of mass matrices, surge-pitch and sway-roll DOFs are decoupled such that their respective RAOs are calculated about a position referred to as the center of rotation (COR) per **Figure 2** [24]. The COR represents the combined mass centroid of the structural mass and added mass in surge (m_{ax}) or sway (m_{ay}), to which their elevations above the keel are:

$$\bar{KR}_x = \frac{m_s \bar{KG} + m_{ax}\left(\frac{D}{2}\right)}{m_s + m_{ax}} \quad , \quad \bar{KR}_y = \frac{m_s \bar{KG} + m_{ay}\left(\frac{D}{2}\right)}{m_s + m_{ay}} \tag{12}$$

where $\bar{KG}$ is the structure's COG above the keel with $\bar{KR}_x$ and $\bar{KR}_y$ denoting the COR location above the keel for surge/pitch and sway/roll DOFs, respectively (see **Figure 2**). The added mass across all DOFs is given by:

$$m_{aR} = \begin{cases} m_{ax} = \frac{1}{2}\rho\pi D^2 B_p, \text{Surge} \\ m_{ay} = \frac{1}{2}\rho\pi D^2 C_p, \text{Sway} \\ m_{az} = \frac{1}{8}\rho\pi B_p^2 C_p C_{zh} C_{zb}, \text{Heave} \\ m_{a\theta_x} = \rho\pi\left[\left(\frac{B_p}{4}\right)^4 + \left(\frac{D}{2}\right)^2\left(\bar{KR}_y - \frac{D}{2}\right)^2\right] C_p, \text{Roll} \\ m_{a\theta_y} = \rho\pi\left[\left(\frac{C_p}{4}\right)^4 + \left(\frac{D}{2}\right)^2\left(\bar{KR}_x - \frac{D}{2}\right)^2\right] B_p, \text{Pitch} \\ m_{a\theta_z} = \frac{\rho\pi D^2}{2}\left(\frac{C_p^3}{12} + \frac{B_p^3}{12}\right), \text{Yaw} \end{cases} \tag{13}$$

with the heave modification factors given by Wang[24] based on experiments done by Brennen[28] being:

$$C_{zh} = \begin{cases} 1.518\left(\frac{h-D}{D}\right)^{-0.365}, \frac{h-D}{D} < 3 \\ 1, \frac{h-D}{D} \geq 3 \end{cases} \tag{14}$$

$$C_{zb} = 1.073\left(\frac{B_p}{D}\right)^{-0.109} \tag{15}$$

where h is the water depth. Note that for translational DOFs (surge, sway, and heave), m_{aR} is simply the total mass of the water volume depicted in **Figure 3**. For rotational DOFs (roll, pitch, and yaw), however, m_{aR} refers to the mass moment of inertia associated with the water volume when taken about an axis passing through the COR. The total hydrodynamic mass mobilized for each DOF is therefore:

$$M_R = \begin{cases} M_x = m_s + m_{ax}, \text{Surge} \\ M_y = m_s + m_{ay}, \text{Sway} \\ M_z = m_s + m_{az}, \text{Heave} \\ M_{\theta_x} = m_{\theta_x} + m_s\left(\bar{KG} - \bar{KR}_y\right)^2 + m_{a\theta_x}, \text{Roll} \\ M_{\theta_y} = m_{\theta_y} + m_s\left(\bar{KG} - \bar{KR}_x\right)^2 + m_{a\theta_y}, \text{Pitch} \\ M_{\theta_z} = m_{\theta_z} + m_{a\theta_z}, \text{Yaw} \end{cases} \tag{16}$$

Here, m_{θ_x}, m_{θ_y}, and m_{θ_z} denote the mass moments of inertia of the MFS taken about the COG in roll, pitch, and yaw, respectively.

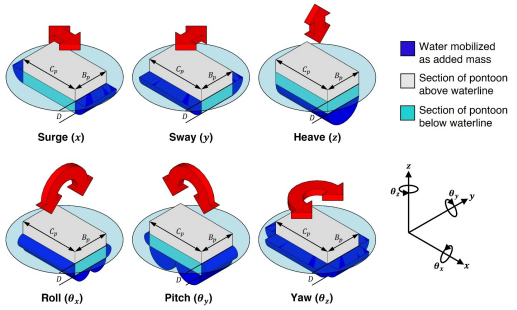

Figure 3. Geometry of added mass for each DOF.

2.3. Wave Forcing

The amplitude of wave forcing (F_{0R}) encapsulates the summation of the Froude-Krylov (F_{FKR}) and added mass (F_{AMR}) forces attracted by the MFS for a given DOF R. Since F_{FKR} and F_{AMR} are harmonically varying with time t, F_{0R} corresponds to time $t = t_0$ where the forcing is at a maximum which is dependent upon the DOF mobilized[26]:

$$F_{0R} = \left|F_{FKR}\left(t_0\right) + F_{AMR}\left(t_0\right)\right|, \quad \begin{cases} t_0 = 0, \text{Heave and yaw} \\ t_0 = -\frac{T}{4}, \text{Surge, sway, pitch, and roll} \end{cases} \tag{17}$$

where $|*|$ signifies the absolute value and $T = 2\pi/\omega$ is the wave period. Equation (17) thus implies that wave forcing is at a maximum for heave and yaw when the crest is directly below the COR whereas for the remaining DOFs, this occurs at the midpoint between a crest and trough. **Figure 4** visualizes the free surface wave profile corresponding to t_0 which is given by:

$$\eta = A\cos\left(kx_\theta - \omega t_0\right) \tag{18}$$

Here, x_θ represents the direction of wave propagation where the origin is defined at the waterplane's geometric centroid. The Froude-Krylov force results from the integration of the dynamic pressure over the wetted surface (S) of the MFS while the added mass forcing is obtained from the acceleration of the added mass:

$$F_{FKR}\left(t_0\right) = \iint_S p_0 dS \tag{19}$$

$$F_{AMR}\left(t_0\right) = m_{aR}a_0 \tag{20}$$

where p_0 is the Airy wave pressure per unit amplitude

($A = 1$) at t_0:

$$p_0\left(x_\theta\right) = \begin{cases} \rho g\left(\frac{\cosh[k(h+z)]}{\cosh(kh)}\right)\cos\left(kx_\theta\right), t_0 = 0 \\ -\rho g\left(\frac{\cosh[k(h+z)]}{\cosh(kh)}\right)\sin\left(kx_\theta\right), t_0 = -T/4 \end{cases} \tag{21}$$

and a_0 is the horizontal (a_{0x}) or vertical (a_{0z}) Airy wave acceleration per unit amplitude ($A = 1$) at t_0:

$$a_{0x}\left(x_\theta\right) = \begin{cases} \omega^2\left(\frac{\cosh[k(h+z)]}{\sinh(kh)}\right)\sin\left(kx_\theta\right), t_0 = 0 \\ \omega^2\left(\frac{\cosh[k(h+z)]}{\sinh(kh)}\right)\cos\left(kx_\theta\right), t_0 = -T/4 \end{cases} \tag{22}$$

$$a_{0z}\left(x_\theta\right) = \begin{cases} -\omega^2\left(\frac{\sinh[k(h+z)]}{\sinh(kh)}\right)\cos\left(kx_\theta\right), t_0 = 0 \\ \omega^2\left(\frac{\sinh[k(h+z)]}{\sinh(kh)}\right)\sin\left(kx_\theta\right), t_0 = -T/4 \end{cases} \tag{23}$$

In Equations (21)–(23), z denotes the vertical elevation above the still water level and $k = 2\pi/L$ is the wavenumber (where L is the wavelength) determined via the dispersion relation:

$$\omega = \sqrt{gk\tanh\left(kh\right)} \tag{24}$$

applicable for all water depths h, or $\omega = \sqrt{gk}$ for deep water conditions ($kh \gg 1$). Alternatively, k can be approximated using:

$$k \approx \frac{\omega^2}{g\sqrt{\tanh\left(\frac{\omega^2 h}{g}\right)}} \tag{25}$$

which is generally accurate to within 10%[29]. Closed-form solutions to Equation (17) applicable for waves approaching from any direction θ taken positive counterclockwise from the x (surge) axis will be presented in the following section for each of the six DOFs.

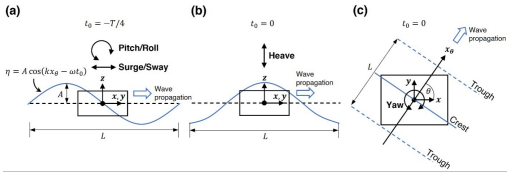

Figure 4. Time corresponding to maximum wave forcing for: (**a**) Surge, sway, roll, pitch; (**b**) Heave; (**c**) Yaw with associated wave profiles.

3. Derivation of Analytical RAO Solutions

The Froude-Krylov (F_{FKR}) and added mass (F_{AMR}) forces exciting each DOF of the MFS are highly dependent upon the direction of wave propagation relative to the pontoon axes. **Figure 2** illustrates the convention adopted in this paper where the angle of wave incidence (θ) is taken positive counterclockwise from the x (surge) axis. Next, it is necessary to define a relationship between the xy axis mapping the coordinates of the pontoon, where $x \in [-C_p/2, C_p/2]$ and $y \in [-B_p/2, B_p/2]$, and the x_θ axis coinciding with the direction of wave propagation (**Figure 2b**). This transformation is given by:

$$x_\theta = x\cos\theta + y\sin\theta \tag{26}$$

For convenience, coordinate transformations for the two longitudinal (x_1 and x_2) and transverse (y_1 and y_2) edges delineating the perimeter of the pontoon (**Figure 2b**) are further listed as:

$$\begin{aligned} x_1 &= x\cos\theta - \tfrac{B_p}{2}\sin\theta \\ x_2 &= x\cos\theta + \tfrac{B_p}{2}\sin\theta \\ y_1 &= y\sin\theta - \tfrac{C_p}{2}\cos\theta \\ y_2 &= y\sin\theta + \tfrac{C_p}{2}\cos\theta \end{aligned} \tag{27}$$

To further simply the analytical expressions presented in this section, the following abbreviations are introduced:

$$\begin{aligned} s_B &= \sin\left(\tfrac{B_p k}{2}\sin\theta\right) \\ s_C &= \sin\left(\tfrac{C_p k}{2}\cos\theta\right) \\ c_B &= \cos\left(\tfrac{B_p k}{2}\sin\theta\right) \\ c_C &= \cos\left(\tfrac{C_p k}{2}\cos\theta\right) \end{aligned} \tag{28}$$

Closed-form solutions to the total forcing amplitude F_{0R} for surge (x), sway (y), heave (z), roll (θ_x), pitch (θ_y), and yaw (θ_z) DOFs will be derived in this section.

3.1. Surge Dynamics

The Froude-Krylov amplitude in surge (F_{FKx}) can be determined via the integration of p_0 corresponding to $t_0 = -T/4$ along the transverse side walls (y_1 and y_2 in **Figure 2b**) of the pontoon:

$$F_{FKx}\left(t_0\right) = \int_{-D}^{0}\int_{-B_p/2}^{B_p/2}\left[p_0\left(y_1\right) - p_0\left(y_2\right)\right]dydz \tag{29}$$

where p_0 is per Equation (21). Evaluating the integrals gives:

$$F_{FKx}\left(t_0\right) = \rho g\zeta_{FKxy}\gamma_{FKx} \tag{30}$$

where:

$$\zeta_{FKxy} = \begin{cases} \frac{\text{sech}(kh)\{\sinh[k(D-h)]+\sinh(kh)\}}{k}, \text{Intermediate water} \\ \frac{1-e^{-kD}}{k}, \text{Deep water}(kh \gg 1) \end{cases} \tag{31}$$

and:

$$\gamma_{FKx} = \frac{4 \csc\theta \, s_B s_C}{k} \tag{32}$$

with s_B and s_C given in Equation (28). The added mass forcing amplitude arises from the integration of a_{0x} (oriented towards the x direction) along the transverse side walls at $z = -D/2$ below the waterplane to represent the approximate centroid of the added mass in surge shown in **Figure 3**. Mathematically, this is expressed as:

$$F_{AMx}(t_0) = \frac{\rho\pi D^2}{4} \int_{-B_p/2}^{B_p/2} [a_{0x}(y_1) + a_{0x}(y_2)] \cos\theta dy \tag{33}$$

where a_{0x} is per Equation (22). Evaluating the integral gives:

$$F_{AMx}(t_0) = \frac{\rho\pi D^2}{4} \omega^2 \zeta_{AMxy} \gamma_{AMx} \cos\theta \tag{34}$$

where:

$$\zeta_{AMxy} = \begin{cases} \frac{\cosh\left[k\left(h-\frac{D}{2}\right)\right]}{\sinh(kh)}, \text{Intermediate water} \\ e^{-\frac{kD}{2}}, \text{Deep water}(kh \gg 1) \end{cases} \tag{35}$$

and:

$$\gamma_{AMx} = \frac{4 \csc\theta \, s_B c_C}{k} \tag{36}$$

with s_B and c_C given in Equation (28). The total forcing amplitude in surge (F_{0x}) can now be determined by substituting Equations (30) and (34) into (17) thus giving the RAO as:

$$RAO_x = \frac{x_0}{A} = \frac{|F_{FKx}(t_0) + F_{AMx}(t_0)|}{M_x \omega^2} \tag{37}$$

where M_x is given in Equation (16).

3.2. Sway Dynamics

The Froude-Krylov amplitude in sway $F_{FKy}(t_0)$ can be determined via the integration of p_0 corresponding to $t_0 = -T/4$ along the longitudinal side walls (x_1 and x_2 in **Figure 2b**) of the pontoon:

$$F_{FKy}(t_0) = \int_{-D}^{0} \int_{-C_p/2}^{C_p/2} [p_0(x_1) - p_0(x_2)] \, dxdz \tag{38}$$

giving:

$$F_{FKy}(t_0) = \rho g \zeta_{FKxy} \gamma_{FKy} \tag{39}$$

where ζ_{FKxy} is per Equation (31) and:

$$\gamma_{FKy} = \frac{4\sec\theta \, s_B s_C}{k} \tag{40}$$

with s_B and s_C given in Equation (28). The added mass forcing amplitude $F_{AMy}(t_0)$ arises from the integration of a_{0x} (oriented towards the y direction) along the longitudinal side walls at $z = -D/2$ below the waterplane to represent the approximate centroid of the added mass in sway shown in **Figure 3**:

$$F_{AMy}(t_0) = \frac{\rho\pi D^2}{4} \int_{-C_p/2}^{C_p/2} [a_{0x}(x_1) + a_{0x}(x_2)] \sin\theta dx \tag{41}$$

Evaluating the integral gives:

$$F_{AMy}(t_0) = \frac{\rho\pi D^2}{4} \omega^2 \zeta_{AMxy} \gamma_{AMy} \sin\theta \tag{42}$$

where ζ_{AMxy} is per Equation (35) and:

$$\gamma_{AMy} = \frac{4 \sec\theta \, c_B s_C}{k} \tag{43}$$

with c_B and s_C given in Equation (28). The total forcing amplitude in sway (F_{0y}) can now be determined by substituting Equations (39) and (42) into (17) thus giving the RAO as:

$$RAO_y = \frac{y_0}{A} = \frac{|F_{FKy}(t_0) + F_{AMy}(t_0)|}{M_y \omega^2} \tag{44}$$

where M_y is given in Equation (16).

3.3. Heave Dynamics

The Froude-Krylov amplitude in heave $F_{FKz}(t_0)$ is determined via the integration of p_0 corresponding to $t_0 = 0$ over the keel of the pontoon located at $z = -D$:

$$F_{FKz}(t_0) = \int_{-B_p/2}^{B_p/2} \int_{-C_p/2}^{C_p/2} p_0(x_\theta) \, dxdy \tag{45}$$

where x_θ is given by Equation (26). Evaluating the integrals produces:

$$F_{FKz}(t_0) = \rho g \zeta_{FKz} \gamma_z \tag{46}$$

with:

$$\zeta_{FKz} = \begin{cases} \frac{\cosh[k(h-D)]}{\cosh(kh)}, \text{Intermediate water} \\ e^{-kD}, \text{Deep water}(kh \gg 1) \end{cases} \quad (47)$$

and:

$$\gamma_z = \frac{4 \csc\theta \sec\theta \, s_B s_C}{k^2} \quad (48)$$

with s_B and s_C given in Equation (28). The added mass forcing amplitude $F_{AMz}(t_0)$ arises from the integration of a_{0z} (vertical acceleration) over the keel of the pontoon ($z = -D$) multiplied by the heave added mass (shown in **Figure 3**) per unit area:

$$F_{AMz}(t_0) = \frac{m_{az}}{B_p C_p} \int_{-B_p/2}^{B_p/2} \int_{-C_p/2}^{C_p/2} a_{0z}(x_\theta) \, dxdy \quad (49)$$

where m_{az} denotes the total heave added mass given in Equation (13). Evaluating the integrals results in:

$$F_{AMz}(t_0) = -\frac{m_{az}}{B_p C_p} \omega^2 \zeta_{AMz} \gamma_z \quad (50)$$

with:

$$\zeta_{AMz} = \begin{cases} \frac{\sinh[k(h-D)]}{\sinh(kh)}, \text{Intermediate water} \\ e^{-kD}, \text{Deep water } (kh \gg 1) \end{cases} \quad (51)$$

and γ_z given by Equation (48). The total forcing amplitude in heave (F_{0z}) can now be determined by substituting Equations (46) and (50) into (17) thus giving the RAO as:

$$RAO_z = \frac{z_0}{A} = \frac{Q_z \left| F_{FKz}(t_0) + F_{AMz}(t_0) \right|}{K_z} \quad (52)$$

where Q_z and K_z are from Equations (6) and (9), respectively.

3.4. Roll Dynamics

The Froude-Krylov moment amplitude in roll $F_{FK\theta_x}(t_0)$ is determined via the integration of p_0 corresponding to $t_0 = -T/4$ over the keel ($z = -D$) multiplied by the y axis distance to the COR. This is combined with the integration of p_0 along the longitudinal side walls (x_1 and x_2 in **Figure 2b**) multiplied with the z axis distance to the COR:

$$F_{FK\theta_x}(t_0) = \int_{-B_p/2}^{B_p/2} \int_{-C_p/2}^{C_p/2} p_0(x_\theta) \, y dxdy + \int_{-D}^{0} \int_{-C_p/2}^{C_p/2} \left[p_0(x_1) - p_0(x_2) \right] (r_{\theta_x} - z) \, dxdz \quad (53)$$

giving:

$$F_{FK\theta_x}(t_0) = \rho g \left(\zeta_{\theta_x} \gamma_{FKy} + \zeta_{FKz} \gamma_{FK\theta_x} \right) \quad (54)$$

where:

$$\zeta_{\theta_x} = \frac{\operatorname{sech}(kh) \left\{ k(D + r_{\theta_x}) \sinh[k(D-h)] - \cosh[k(h-D)] + k r_{\theta_x} \sinh(kh) \right\} + 1}{k^2} \quad (55)$$

for intermediate water or:

$$\zeta_{\theta_x} = \frac{e^{-kD} \left[e^{kD}(k r_{\theta_x} + 1) - k(D + r_{\theta_x}) - 1 \right]}{k^2} \quad (56)$$

for deep water conditions ($kh \gg 1$). γ_{FKy} and ζ_{FKz} are given by Equations (40) and (47), respectively, and:

$$r_{\theta_x} = \bar{KR}_y - D \quad (57)$$

is the elevation of the COR in roll above the waterplane with $\bar{KR}_y$ determined using Equation (12). Additionally:

$$\gamma_{FK\theta_x} = \frac{2 s_C \csc\theta \sec\theta \, (B_p k c_B - 2 s_B \csc\theta)}{k^3} \quad (58)$$

where s_B, s_C, and c_B presented via Equation (28). The added mass moment amplitude in roll stems from the integration of the vertical acceleration (a_{0z}) longitudinally along the keel ($z = -D$) at $y = \pm B_p/4$ to coincide with the centroid of the semicircular prismatic volumes shown in **Figure 3**. This acceleration is multiplied by the corresponding added mass (treated as a lumped mass) and its y axis distance from the COR ($B_p/4$) in order to yield the added mass moment in roll. To account for the added mass along the longitudinal side walls, the horizontal acceleration (a_{ox}) oriented towards the y direction is integrated along x_1 and x_2 (see **Figure 2b**) at $z = -D/2$ and multiplied with the added mass and its z axis distance to the COR to produced the roll added

mass moment induced by fluid acceleration along the side walls. Mathematically, the total added mass moment in roll is expressed as:

$$F_{AM\theta_x}(t_0) = \frac{\rho\pi B_p^2}{32}\left(\frac{B_p}{4}\right)\int_{-C_p/2}^{C_p/2}\left[a_{0z}\left(x\cos\theta + \frac{B_p}{4}\sin\theta\right) - a_{0z}\left(x\cos\theta - \frac{B_p}{4}\sin\theta\right)\right]dx + \frac{\rho\pi D^2}{8}\left(\frac{D}{2} + r_{\theta_x}\right)\int_{-C_p/2}^{C_p/2}\left[a_{0x}(x_1) + a_{0x}(x_2)\right]sin\theta dx \tag{59}$$

Note that the first term on the right-hand side of Equation (59) reflects the moment produced by the added mass on the keel and the second term accounts for the moment resulting from the added mass along the longitudinal side walls. Evaluating (59) yields:

$$F_{AM\theta_x}(t_0) = \frac{\rho\pi\omega^2}{8}\left[\frac{B_p^2}{4}\zeta_{AMz}\gamma_{AM\theta_x} + D^2\left(\frac{D}{2} + r_{\theta_x}\right)\zeta_{AMxy}\gamma_{AMy}\sin\theta\right] \tag{60}$$

where r_{θ_x} is from Equation (57). ζ_{AMxy}, ζ_{AMz}, and γ_{AMy} are given by Equations (35), (51), and (43), respectively, and:

$$\gamma_{AM\theta_x} = \frac{B_p s_C \sec\theta \sin\left(\frac{B_p k}{4}\sin\theta\right)}{k} \tag{61}$$

with s_C per Equation (28). The total forcing amplitude in roll ($F_{0\theta_x}$) can now be determined by substituting Equations (54) and (60) into (17) thus giving the RAO (in rad/m) as:

$$RAO_{\theta_x} = \frac{\theta_{x0}}{A} = \frac{Q_{\theta_x}\left|F_{FK\theta_x}(t_0) + F_{AM\theta_x}(t_0)\right|}{K_{\theta_x}} \tag{62}$$

where Q_{θ_x} and K_{θ_x} are from Equations (6) and (9), respectively.

3.5. Pitch Dynamics

Similar to roll, the Froude-Krylov moment amplitude in pitch $F_{FK\theta_y}(t_0)$ is:

$$F_{FK\theta_y}(t_0) = -\rho g\left(\zeta_{\theta_y}\gamma_{FKx} + \zeta_{FKz}\gamma_{FK\theta_y}\right) \tag{63}$$

where:

$$\zeta_{\theta_y} = \frac{\operatorname{sech}(kh)\left\{k\left(D + r_{\theta_y}\right)\sinh\left[k(D-h)\right] - \cosh\left[k(h-D)\right] + kr_{\theta_y}\sinh(kh)\right\} + 1}{k^2} \tag{64}$$

for intermediate water or:

$$\zeta_{\theta_y} = \frac{e^{-kD}\left[e^{kD}\left(kr_{\theta_y} + 1\right) - k\left(D + r_{\theta_y}\right) - 1\right]}{k^2} \tag{65}$$

for deep water conditions ($kh \gg 1$). γ_{FKx} and ζ_{FKz} are given by Equations (32) and (47), respectively, and:

$$r_{\theta_y} = \bar{KR}_x - D \tag{66}$$

is the elevation of the COR in pitch above the waterplane with $\bar{KR}_x$ determined using Equation (12). Additionally:

$$\gamma_{FK\theta_y} = \frac{2s_B\csc\theta\sec\theta\left(C_p k c_C - 2s_C\sec\theta\right)}{k^3} \tag{67}$$

where s_B, s_C, and c_C presented via Equation (28). Following the same integral approach as described previously for roll (not repeated for brevity), the total added mass moment in pitch is expressed as:

$$F_{AM\theta_y}(t_0) = -\frac{\rho\pi\omega^2}{8}\left[\frac{C_p^2}{4}\zeta_{AMz}\gamma_{AM\theta_y} + D^2\left(\frac{D}{2} + r_{\theta_y}\right)\zeta_{AMxy}\gamma_{AMx}\cos\theta\right] \tag{68}$$

where r_{θ_y} is from Equation (66). ζ_{AMxy}, ζ_{AMz}, and γ_{AMx} are given by Equations (35), (51), and (36), respectively, and:

$$\gamma_{AM\theta_y} = \frac{C_p s_B \csc\theta \sin\left(\frac{C_p k}{4}\cos\theta\right)}{k} \tag{69}$$

with s_B per Equation (28). The total forcing amplitude in roll ($F_{0\theta_y}$) can now be determined by substituting Equations (63) and (68) into (17) thus giving the RAO (in rad/m) as:

$$RAO_{\theta_y} = \frac{\theta_{y0}}{A} = \frac{Q_{\theta_y}\left|F_{FK\theta_y}(t_0) + F_{AM\theta_y}(t_0)\right|}{K_{\theta_y}} \tag{70}$$

where Q_{θ_y} and K_{θ_y} are from Equations (6) and (9), respectively.

3.6. Yaw Dynamics

The Froude-Krylov moment amplitude in yaw $F_{FK\theta_Z}$ arises from the integration of p_0 around the perimeter of the pontoon (x_1, x_2, x_3, and x_4) multiplied by the perpendicular lever arm (x or y) to the z axis:

$$F_{FK\theta_z}(t_0) = \int_{-D}^{0}\int_{-C_p/2}^{C_p/2}[p_0(x_1) - p_0(x_2)]\,x\,dx\,dz + \int_{-D}^{0}\int_{-B_p/2}^{B_p/2}[p_0(y_2) - p_0(y_1)]\,y\,dy\,dz \tag{71}$$

where the first and second terms on the right-hand side of Equation (71) represent the dynamic wave pressure acting on the longitudinal and transverse side walls, respectively. Resolving the integrals yield:

$$F_{FK\theta_z}(t_0) = \rho g \zeta_{FKxy}(\gamma_{FKx} + \gamma_{FKy}) \tag{72}$$

with ζ_{FKxy}, γ_{FKx}, and γ_{FKy} respectively given by Equations (31), (32), and (40). Likewise, the yaw added mass moment amplitude results from the prismatic added mass distribution shown in **Figure 3** accelerated along the perimeter of the pontoon (normal to the side walls) multiplied by the perpendicular lever arm (x or y) to the z axis:

$$F_{AM\theta_z}(t_0) = \frac{\rho\pi D^2}{4}\int_{-C_p/2}^{C_p/2}[a_{0x}(x_1) + a_{0x}(x_2)]\,x\sin\theta\,dx - \frac{\rho\pi D^2}{4}\int_{-B_p/2}^{B_p/2}[a_{0x}(y_1) + a_{0x}(y_2)]\,y\cos\theta\,dy \tag{73}$$

Here, the first and second terms on the right-hand side represent the yaw moment induced by the added mass on the longitudinal and transverse side walls, respectively. Evaluating Equation (73) at $z = -D/2$ yields:

$$F_{AM\theta_z}(t_0) = \frac{\rho\pi D^2}{4}\omega^2\zeta_{AMxy}(\gamma_{AMx}\sin\theta - \gamma_{AMy}\cos\theta) \tag{74}$$

where ζ_{AMxy}, γ_{AMx}, and γ_{AMy} are given in Equations (35), (36), and (43). The total forcing amplitude in yaw ($F_{0\theta_z}$) can now be determined by substituting Equations (72) and (74) into (17) thus giving the RAO (in rad/m) as:

$$RAO_{\theta_z} = \frac{\theta_{z0}}{A} = \frac{|F_{FK\theta_z}(t_0) + F_{AM\theta_z}(t_0)|}{M_{\theta_z}\omega^2} \tag{75}$$

with the total yaw mass M_{θ_z} obtained from Equation (16).

4. Summary of Calculation Procedure

The determination of RAOs pertaining to each DOF R for a symmetrically loaded rectangular pontoon via the analytical approach developed in this work is summarized in **Figure 5**. Relevant equations giving the dynamic properties used in the calculations are listed in **Table 1**. After identifying the structural and wave characteristics, dynamic properties independent of wave directionality encompassing the waterplane stiffness (K_R), total hydrodynamic mass (M_R), and the dynamic amplification factor (Q_R) may be obtained (step 1 in **Figure 5**). Note that K_R and Q_R are only relevant for stiffness-dominated DOFs where $R = \{z, \theta_x, \theta_y\}$. Next, the total forcing amplitude, comprising Froude-Krylov (F_{FKR}) and added mass (F_{AMR}) components, are computed which are dependent upon the direction of wave propagation (θ) for each DOF R (step 2 in **Figure 5**). Due to the double symmetry of the pontoon, the angle of wave incidence need only be taken between 0° and 90°. However, for purely longitudinal ($\theta = 0°$) for transverse ($\theta = 90°$) waves, the closed-form expressions presented in Sections 3.1–3.6 may result in singularities. To mitigate this phenomenon, the following adjustments are adopted for the treatment of θ:

$$\theta = \begin{cases} \epsilon, \theta = 0° \\ 90° - \epsilon, \theta = 90° \\ \theta, 0° < \theta < 90° \end{cases} \tag{76}$$

where ϵ represents an arbitrarily small positive quantity (e.g., $\epsilon = 10^{-6}$). After solving for the quantities listed in steps 1 and 2, the RAO (as a function of the wave frequency ω or period T) for each DOF R may be determined using the equations appropriate for mass- (surge, sway, and yaw) or stiffness- (heave, roll, and pitch) dominated DOFs as specified in step 3 of **Figure 5**. Evidently, the rigid body response of an MFS excited by regular waves with amplitude A given by Equation (4) can be directly inferred from the RAOs. Here, the response amplitude R_0 is simply the corresponding RAO multiplied by the wave amplitude $R_0 = RAO_R \times A$ per Equation (2). The RAOs determined in accordance with **Figure 5**

Table 1. Summary of equations used to determine the RAO across all DOFs.

Dynamic Property	Degree of freedom R =					
	x (Surge)	y (Sway)	z (Heave)	θ_x (Roll)	θ_y (Pitch)	θ_z (Yaw)
K_R	-	-	Eq. (9)	Eq. (9)	Eq. (9)	-
M_R	Eq. (16)	Eq. (16)	Eq. (16)	Eq. (16)	Eq. (16)	Eq. (16)
Q_R	-	-	Eq. (6)	Eq. (6)	Eq. (6)	-
F_{FKR}	Eq. (30)	Eq. (39)	Eq. (46)	Eq. (54)	Eq. (63)	Eq. (72)
F_{AMR}	Eq. (33)	Eq. (42)	Eq. (50)	Eq. (60)	Eq. (68)	Eq. (74)
RAO$_R$	Eq. (37)	Eq. (44)	Eq. (52)	Eq. (62)	Eq. (70)	Eq. (75)

may also be combined with various wave spectra (e.g., JONSWAP) to yield the dynamic response under irregular waves [30, 31].

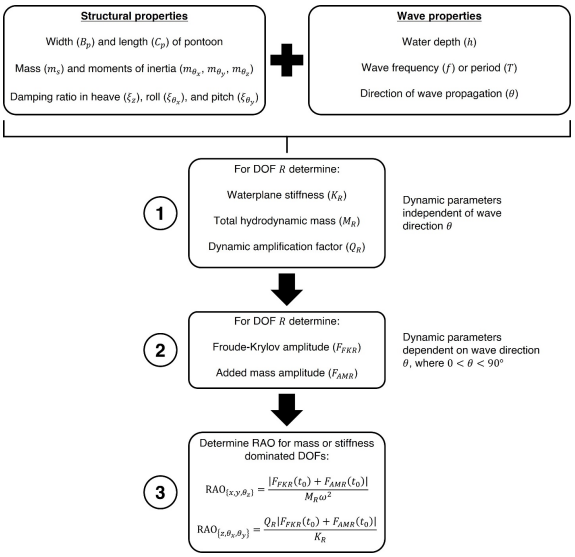

Figure 5. RAO calculation procedure for DOFs $R = \{x, y, z, \theta_x, \theta_y, \theta_z\}$.

5. Validation of Analytical Solutions

In order to validate the derivations presented in this paper, the closed-form expressions describing the rigid body dynamics of an MFS about all six DOFs excited by waves traveling along any arbitrary direction were benchmarked against numerical simulations performed using the commercial software ANSYS/AQWA. The validation was conducted across two different MFS prototypes documented in the literature. In addition, both prototypes are assumed to exist in water h = 18 m deep to reflect a typical site near Singapore as adopted by Ren et al. [17]. A description of each MFS is subsequently presented followed by comparisons of the RAO between analytical and numerical results.

5.1. Description of MFS Prototypes

The structural configuration of MFS A (**Figure 6a**) is based on a two-story floating house proposed by Nakajima et al. [32]. The rectangular pontoon measures 6.2 m in length, 5 m in width, and 1.5 m in depth, and supports a single rectangular house 4.5 m (L) × 5 m (W) × 3 m (H). The mass of the house and pontoon are 16500 kg and 7900 kg, respectively, thus giving a total MFS mass of m_s = 24400 kg. This confers a draft of D = 0.77 m, being approximately 51% of the total pontoon depth. When assuming that the building and pontoon masses are uniformly distributed, the COG of the MFS lies 2.27 m above the keel (**Table 2**). The MFS mass moments of inertia in roll (m_{θ_x}), pitch (m_{θ_y}), and yaw (m_{θ_z}) were also calculated based on the uniform distribution of the pontoon and building masses and are summarized in **Table 2**.

The pontoon dimensions of MFS B (**Figure 6b**) are based on the Pier 21 floating restaurant (constructed in 1991) currently docked in Yokohama, Japan. According to Watanabe et al. [10], the square pontoon exhibits dimensions of 24 m (L) × 24 m (W) × 3.2 m (H). While the mass is not known, a density of 170 kgm-3 is assumed for the pontoon to match that of MFS A. Likewise, the building is approximated as a cube with each side measuring 15 m and displaying an average density of 244 kgm-3 based on MFS A. This resulted in pontoon and building masses of 3.13 × 105 kg and 8.24 × 105 kg, respectively, yielding a combined mass of m_s = 1.14 × 106 kg. The corresponding draft of D = 1.93 m is shown to be approximately 60% of the pontoon depth. When assuming that the pontoon and building masses are uniformly distributed, a COG of 8.19 m above the keel is produced.

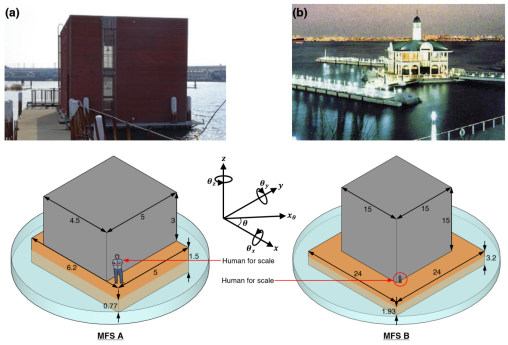

Figure 6. Photographic image and geometric properties of: (**a**) MFS A; (**b**) MFS B prototypes adopted for the validation study. All dimensions in meters.

5.2. Comparison with Potential Theory

The closed-form RAO expressions derived in this paper were subsequently evaluated against numerical solutions incorporating hydrodynamic diffraction analysis to ascertain their performance as a preliminary tool for the prototyping of pontoon-supported floating structures. The commercial BEM software ANSYS/AQWA was adopted to calculate the RAO across all six DOFs for the two MFS designs detailed in Section 5.1. Based on potential flow theory, AQWA has been widely used in the naval and offshore industries for the modeling of pontoon, semi-submersible, and other marine vessels [33–35]. Five wave incidence angles of θ = 0°, 25°, 45°, 65°, and 90° were selected to cover a representative range of wave directions while the water depth was kept constant at h = 18 m for all cases. Wave periods between 5 and 20 s were considered which is consistent with Wang [23]. Note that the RAOs for surge (x) and sway (y) computed via ANSYS/AQWA were taken at the structure's COG. This contrasts with the analytical method where surge and sway RAOs are calculated about the COR for surge/pitch and sway/roll, respectively, which is located slightly below the COG (see **Figure 2**).

Figure 7 presents the comparison between analytical (solid line) and numerical (discrete points) results for MFS A (**Figure 6a**). It is seen that the closed-from RAO expressions were closely synchronized with numerical predictions across all DOFs and wave directions. For stiffness-dominated motions (heave, roll, and pitch), damping ratios of 0.1 were adopted to achieve the most reliable comparison with numerical solutions and are consistent with recommendations by Wang [24]. Yet, damping represents a highly nonlinear and complex phenomenon that is also frequency dependent. In addition to the pontoon's geometry, the damping ratio is influenced by factors including skin friction, eddy shedding, wave parameters, lift effects, and the presence of motion stabilizers such as bilge keels [36]. Nevertheless, **Figure 7** demonstrates that a constant damping ratio for each stiffness-dominated DOF can be utilized to effectively capture the damping associated with heave, roll, and pitch motions for the MFS examined. In addition, RAOs for surge and sway calculated at the COG (numerical) and COR (analytical) are also highly comparable. This is due to their relatively close proximity with $\bar{KG}$, $\bar{KR}_x$, and $\bar{KR}_y$ being 2.27 m, 1.96 m, and 1.90 m, respectively (**Table 2**). Note that discrepancies between surge/sway RAOs calculated at the COG and COR are increased for wave periods yielding large pitch/roll RAOs. This can be observed in **Figure 7b** for T = 6 s which coincides with the roll natural period.

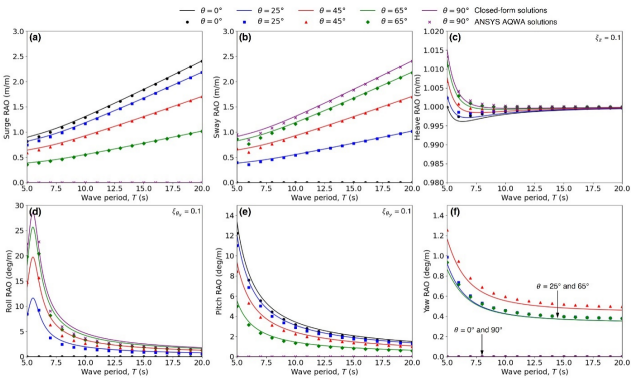

Figure 7. Comparison between closed-form and numerical RAOs for MFS A across: (**a**) Surge; (**b**) Sway; (**c**) Heave; (**d**) Roll; (**e**) Pitch; (**f**) Yaw DOFs.

Figure 8 summarizes the comparison between analytical and numerical RAO solutions for MFS B (**Figure 6b**). Similar to MFS A, closed-form and ANSYS/AQWA results are closely synchronized across all DOFs and wave directions considered. Since the pontoon is square in shape, only θ = 25° and 65° yield non-zero RAOs for yaw (**Figure 8f**), which are also identical due to symmetry. Likewise, the square pontoon translates to identical heave RAOs over all wave directions. Furthermore, sway and surge RAOs computed about the COG and COR for numerical and analytical methods, respectively, are largely consistent due to their close proximity (**Table 2**). While

Table 2. Summary of structural properties corresponding to each MFS adopted for the validation study.

MFS Type	C_p (m)	B_p (m)	m_s (kg)	m_{θ_x} (kgm^2)	m_{θ_y} (kgm^2)	m_{θ_z} (kgm^2)	$\bar{KG}$ (m)	$\bar{KR}_x$ (m)	$\bar{KR}_y$ (m)
A	6.2	5	24400	91730	94050	103980	2.27	1.96	1.90
B	24	24	1.14×10^6	6.5×10^7	6.5×10^7	6.1×10^7	8.19	7.38	7.38

a damping ratio of 0.1 was adopted for heave (ξ_z), it is observed that a damping ratio of 0.05 is more applicable to roll (ξ_{θ_x}) and pitch (ξ_{θ_y}) for MFS B based on curve-fitting.

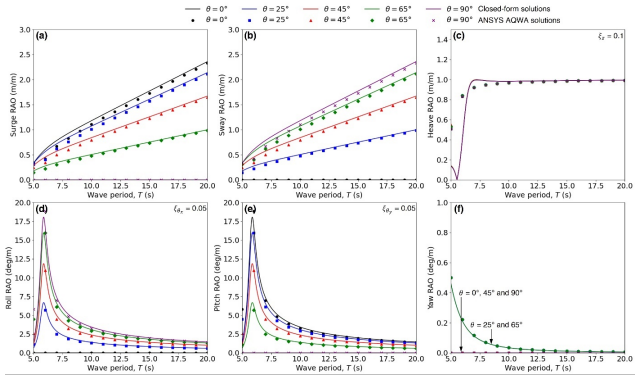

Figure 8. Comparison between closed-form and numerical RAOs for MFS B across: (**a**) Surge; (**b**) Sway; (**c**) Heave; (**d**) Roll; (**e**) Pitch; (**f**) Yaw DOFs.

6. Parametric Investigation

A parametric investigation was subsequently conducted to explore how different structural geometries and angles of wave incidence influence the accelerations experienced by an MFS under realistic sea states given by a wave spectrum. Determining building accelerations (both horizontal and vertical) is important as this informs the assessment of occupant comfort per guidelines such as ISO 10137 [37]. The structure examined was based on MFS B (**Figure 6b**) where its pontoon dimensions were kept constant (C_p = B_p = 24 m). The length (C_b) and width (B_b) of the building were varied as a ratio of the pontoon's length (C_p) and width (B_p) to cover a range between 0.4 and 1.0. To ensure that the total MFS mass (and hence its draft) remains unchanged, a constant building volume of 3375 m3 (matching **Figure 6b**) was imposed. Hence, the lower limit for B_b/B_p and C_b/C_p of 0.4 was provided to avoid static instability due to the structure becoming excessively tall. **Figure 9** summarizes the building height (D_b) as a function of its B_b/B_p and C_b/C_p ratios.

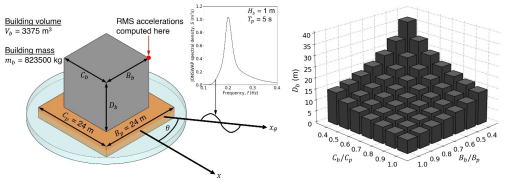

Figure 9. Geometric description of MFS considered for the parametric study with building height (D_b) plotted as a function of B_b/B_p and C_b/C_p.

6.1. RMS Acceleration Under Irregular Waves

Irregular waves corresponding to a 1-year storm as reported by Ren et al. [14] with significant wave height H_s = 1 m and peak period T_p = 5 s (water depth 18 m) were selected as the excitation source. The wave spectral density (S_J) as a function of frequency (f) was determined according to the JONSWAP spectrum [28] and plotted in **Figure 9**:

$$S_J(f) = \beta_J H_s^2 \left(\frac{f_p^4}{f^5}\right) \exp\left[-1.25\left(\frac{f_p}{f}\right)^4\right] \gamma_J^{\exp\left[\frac{-\left(\frac{f}{f_p}-1\right)^2}{2\sigma_J^2}\right]} \tag{77}$$

with the JONSWAP parameters being:

$$\beta_J = \frac{0.0624[1.094-0.01915\ln(\gamma_J)]}{0.230+0.0336\gamma_J-0.185(1.9+\gamma_J)^{-1}}$$
$$\sigma_J = \begin{cases} 0.07, f \leq f_p \\ 0.09, f > f_p \end{cases} \tag{78}$$
$$\gamma_J = 3.3$$

where $f_p = 1/T_p$ is the frequency of the spectral peak. Using Equation (77) and the RAOs calculated from **Figure 5**, the root mean square (RMS) acceleration at the COR associated with each DOF R (G_R) can be determined via [30]:

$$G_R = \sqrt{\sum_{i=1}^{N} S_J(f_i)\left[\omega_i^2 \mathrm{RAO}_R(f_i)\right]^2 \Delta f} \tag{79}$$
$$\text{where } R = \{x, y, z, \theta_x, \theta_y, \theta_z\}$$

This equation was solved by discretizing the wave spectrum (**Figure 9**) into N = 200 uniform frequency bands Δf wide, with f_i denoting the frequency of band

i and $\omega_i = 2\pi f_i$. Since the maximum and minimum frequencies are selected to be 0.4 and 0.1 Hz, respectively, Δf = (0.4 – 0.1)/200 = 0.0015 Hz. In this study, the horizontal and vertical RMS accelerations were computed at the top corner of the building (shown in **Figure 9**) as this represents the most critical location. Since horizontal motions are produced by surge (x), sway (y), roll (θ_x), pitch (θ_y), and yaw (θ_z), the resultant RMS horizontal acceleration (G_h) can be obtained through mean square addition of each individual component[38]:

$$G_h = \sqrt{G_x^2 + G_y^2 + G_{\theta_x^h}^2 + G_{\theta_y^h}^2 + G_{\theta_z^h}^2} \tag{80}$$

where:

$$\begin{aligned} G_{\theta_x^h} &= G_{\theta_x}\left(D_b + D_p - \bar{K}R_y\right) \\ G_{\theta_y^h} &= G_{\theta_y}\left(D_b + D_p - \bar{K}R_x\right) \\ G_{\theta_z^h} &= G_{\theta_z}\sqrt{\left(\tfrac{B_b}{2}\right)^2 + \left(\tfrac{C_b}{2}\right)^2} \end{aligned} \tag{81}$$

denote the horizontal RMS acceleration produced by roll, pitch, and yaw components, respectively, at the location specified in **Figure 9**. Likewise, the RMS vertical acceleration (G_v) results from heave, roll, and pitch components:

$$G_v = \sqrt{G_z^2 + G_{\theta_x^v}^2 + G_{\theta_y^v}^2} \tag{82}$$

where:

$$\begin{aligned} G_{\theta_x^v} &= G_{\theta_x}\left(\tfrac{B_b}{2}\right) \\ G_{\theta_y^v} &= G_{\theta_y}\left(\tfrac{C_b}{2}\right) \end{aligned} \tag{83}$$

give the vertical RMS acceleration produced by roll and pitch at the corner, respectively.

6.2. Parametric Results

Figure 10 presents the RMS horizontal (G_h) and vertical (G_v) acceleration at the building's upper corner as a function of B_b/B_p and C_b/C_p across five wave incidence angles of θ = 0°, 22.5°, 45°, 67.5°, and 90° taken counterclockwise about the x axis (**Figure 9**). It is seen that the largest RMS accelerations occur for orthogonal wave directions (θ = 0° and 90°) while θ = 45° yields the smallest. For both G_h and G_v, a slender superstructure with B_b/B_p = C_b/C_p = 0.4 (building height D_b = 36.6 m) is observed to produce the lowest values. This seemingly counterintuitive response is due to its roll and pitch natural frequency of 0.09 Hz (**Figure 11**) being significantly lower than the frequency of the spectral peak f_p = 0.2 Hz, thus minimizing the contribution of rotational motion to G_h and G_v. On the contrary, B_b/B_p = C_b/C_p = 1.0 witnessed the largest G_v (**Figure 10f,j**) while G_h remains relatively small. This response is explained by the location's long horizontal lever-arm from the COR in roll and pitch exacerbated by their natural frequencies being in close proximity to f_p amplifying vertical motions. Likewise, the much shorter vertical lever-arm acts to minimize rotational contributions to horizontal motion. As seen in **Figure 10a,e**, the greatest horizontal accelerations are produced when orthogonal waves excite the structure perpendicular to the largest B_b/B_p or C_b/C_p ratio of 1.0, while the other dimension is at its smallest of 0.4. This effect is explained again via **Figure 11** which implies significant rotational contributions to horizontal motion due to the closeness of $f_{n\theta_x}$ and $f_{n\theta_y}$ (around 0.18 Hz) to the spectral peak. Ultimately, this parametric study highlighted the intricate relationship between a floating structure's natural frequency, wave spectra, directionality, and superstructure geometry on its overall dynamic response within a purely analytical framework.

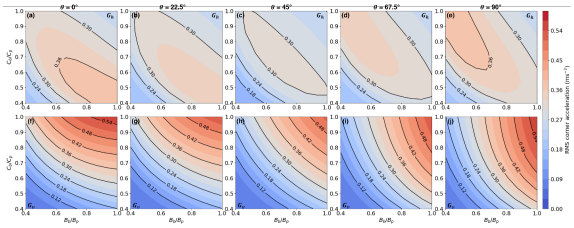

Figure 10. RMS horizontal corner acceleration (G_h) for wave incidence angles. (**a**) 0°; (**b**) 22.5°; (**c**) 45°; (**d**) 67.5°; (**e**) 90°. RMS vertical corner acceleration (G_v) for wave incidence angles. (**f**) 0°; (**g**) 22.5°; (**h**) 45°; (**i**) 67.5°; (**j**) 90°.

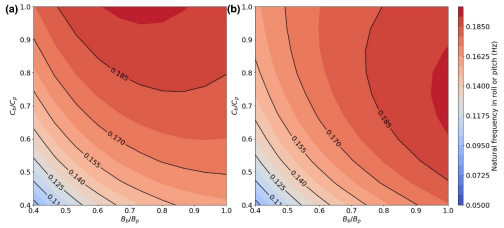

Figure 11. Natural frequencies for: (**a**) Roll; (**b**) Pitch.

7. Conclusions

The adoption of modular floating structures (MFS) as a sustainable alternative to traditional methods of

land reclamation has gained significant attention in recent years due to the increasing hazards posed by climate change. As such, it is imperative that simplified methods of dynamic analyses are developed for the prototyping of potential structural designs as a precursor to detailed numerical modeling. This paper proposed closed-form solutions describing the 3D rigid body response of an MFS across all six degrees of freedom (DOF) excited by surface waves approaching from any arbitrary direction within water of any depth. The expressions were derived based on a symmetrically loaded rectangular pontoon interacting with linear waves assuming frequency-independent added mass and damping. To evaluate its performance, the analytical approach was implemented to predict the 6-DOF response amplitude operators (RAO) of two MFS prototypes, referenced as MFS A and B, respectively. RAO solutions were subsequently benchmarked against numerical hydrodynamic diffraction analysis performed using ANSYS/AQWA across five wave directions between 0° (longitudinal) and 90° (transverse). The comparison confirmed that the closed-form equations generally performed well across both MFS configurations, five angles of wave incidence, six DOFs, and wave periods between 5 and 20 s. A parametric study revealed the contribution of wave directionality and structural geometry to the dynamic accelerations experienced by a floating structure excited by irregular waves. Additional conclusions from this study are as follows:

Based on the MFS designs examined, damping ratios between 0.05 and 0.1 are recommended for roll (ξ_{θ_x}) and pitch (ξ_{θ_y}) DOFs while a ratio of ξ_{θ_z} = 0.1 may be adopted to model the heave response.

The closed-form solutions were highly synchronized with numerical results for mass-dominated DOFs (surge, sway, and yaw) across both MFS configurations, wave directions, and periods considered.

In general, the surge and sway response calculated analytically about the center of rotation (COR) can reliably approximate surge and sway motions about the MFS center of gravity (COG). However, this approximation should be used with caution if the distance between the COR and COG is large or if large roll/pitch RAOs are predicted.

For a superstructure supported by a square pontoon, the largest horizontal and vertical RMS accelerations are triggered by orthogonal waves exhibiting a spectral peak in close proximity to the roll/pitch natural frequency, thus emphasizing their importance to the overall dynamic response.

Ultimately, the closed-form solutions introduced in this paper serve as useful tools for architects and structural engineers involved with the design of floating structures. It is hoped that this generalized framework will encourage the exploration of novel and sustainable floating solutions to achieve more resilient and climate-adaptable future cities.

Funding

This work received no external funding.

Institutional Review Board Statement

Not applicable.

Informed Consent Statement

Not applicable.

Data Availability Statement

Data will be made available on request.

Conflicts of Interest

The author declares no conflict of interest.

References

[1] Brown, S., Nicholls, R.J., Woodroffe, C.D., et al., 2013. Sea-level rise impacts and responses: a global perspective. In: Finkl, C.W. (ed.). Coastal Hazards. Springer: Dordrecht, The Netherlands. pp. 117–149.

[2] Small, C., Nicholls, R.J., 2003. A global analysis of human settlement in coastal zones. Journal of Coastal Research. 19(3), 584–599.

[3] United Nations, 2017. Factsheet: people and oceans. The Ocean Conference; June 5–9, 2017;

New York, USA. pp. 1–2.

[4] Globalization and World Cities, 2023. Globalization and World Cities Research Network. Available from: https://gawc.lboro.ac.uk/gawc-worlds/the-world-according-to-gawc/world-cities-2024/ (cited 31 May 2023).

[5] Neumann, B., Vafeidis, A.T., Zimmermann, J., et al., 2015. Future coastal population growth and exposure to sea-level rise and coastal flooding - a global assessment. Public Library of Science One. 10(3), e0118571.

[6] Bamber, J.L., Oppenheimer, M., Kopp, R.E., et al., 2019. Ice sheet contributions to future sea-level rise from structured expert judgment. Proceedings of the National Academy of Sciences. 116(23), 11195–11200.

[7] Nicholls, R.J., Marinova, N., Lowe, J.A., et al., 2011. Sea-level rise and its possible impacts given a 'beyond 4°C world' in the twenty-first century. Philosophical Transactions of the Royal Society A: Mathematical, Physical and Engineering Sciences. 369(1934), 161–181.

[8] Mohammed, A., 2019. Sustainable floating cities can offer solutions to climate change threats facing urban areas, deputy secretary-general tells first high-level meeting. Available from: https://press.un.org/en/2019/dsgsm1269.doc.htm (cited 31 May 2023).

[9] American Society of Civil Engineers, 2019. Future world vision: infrastructure reimagined. Available from: https://futureworldvision.org/ (cited 31 May 2023).

[10] Watanabe, E., Wang, C.M., Utsunomiya, T., et al., 2004. Very large floating structures: applications, analysis and design. 2004–02.

[11] Hadary, T., Martinez, J.G., Sella, I., et al., 2022. Eco-engineering for climate change - floating to the future. Proceedings of the Second World Conference on Floating Solutions, Rotterdam; October 27–29, 2020; Rotterdam, Netherlands (Rotterdam, NL). pp. 409–421.

[12] Wang, C.M., Watanabe, E., Utsunomiya, T., 2008. Very Large Floating Structures. Chemical Rubber Company Press: Boca Raton, Florida, USA. pp. 11.

[13] Bandrowski, T.J., 2015. Lily Pad Urbanism: Reimagining Seattle's Floating Home Community [Master's dissertation]. Seattle, WA: University of Washington. p. 11.

[14] Blanco, L.F.L., Hancco, R.W.M., 2020. Modeling and forecasting international tourism demand in Puno-Peru. Revista Brasileira de Pesquisa em Turismo. 14(1), 34–55.

[15] Lin, Z., 2007. Urban structure for the expanding metropolis: Kenzo Tange's 1960 plan for Tokyo. Journal of Architectural and Planning Research. 24(2), 109–124.

[16] Cebada-Relea, A.J., Lopez, M., Aenlle, M., 2022. Time-domain numerical modelling of the connector forces in a modular pontoon floating breakwater under regular and irregular oblique waves. Ocean Engineering. 243, 110263.

[17] Ren, N., Zhang, C., Magee, A.R., et al., 2019. Hydrodynamic analysis of a modular multi-purpose floating structure system with different outermost connector types. Ocean Engineering. 176, 158–168.

[18] Gutierrez-Romero, J.E., Garcia-Espinosa, J., Servan-Camas, B., et al., 2016. Non-linear dynamic analysis of the response of moored floating structures. Marine Structures. 49, 116–137.

[19] Rahman, M.A., Mizutani, N., Kawasaki, K., 2006. Numerical modeling of dynamic responses and mooring forces of submerged floating breakwater. Coastal Engineering. 53(10), 799–815.

[20] Bouscasse, B., Colagrossi, A., Marrone, S., et al., 2013. Nonlinear water wave interaction with floating bodies in SPH. Journal of Fluids and Structures. 42, 112–129.

[21] Dominguez, J.M., Crespo, A.J., Hall, M., et al., 2019. SPH simulation of floating structures with moorings. Coastal Engineering. 153, 103560.

[22] Takabatake, H., 2015. A simplified analysis of rectangular floating plates subjected to moving loads. Ocean Engineering. 97, 37–47.

[23] Wang, S., 2023. Simplified analytical solutions to the yaw dynamics of modular floating structures. Ocean Engineering. 276, 114206.

[24] Wang, S., 2022. Analytical solutions for the dynamic analysis of a modular floating structure for urban expansion. Ocean Engineering. 266, 112878.

[25] Suzuki, H., Yoshida, K., 1996. Design flow and strategy for safety of very large floating structure. Proceedings of the International Workshop on Very Large Floating Structures; April 24–26, 1996; Hayama, Japan (Hayama, Kanagawa). pp. 21–27.

[26] Barltrop, N.D.P., 1998. Floating Structures: A Guide for Design and Analysis. Oilfield Publications Limited: Ledbury, UK. pp. 471–514.

[27] Vugts, J.H., 1968. The hydrodynamic coefficients for swaying, heaving, and rolling cylinders in a free surface. International Shipbuilding Progress. 15(167), 251–276.

[28] C. E. Brennen, 1982. A review of added mass and fluid inertial forces. 82.010, January 1982.

[29] United States Army Corps of Engineers, 2012. Coastal Engineering Manual. USACE: Washington, DC, USA. Part II, Chapter 1, p. 13.

[30] Faltinsen, O., 1993. Sea Loads on Ships and Offshore Structures. Cambridge University Press: Cambridge, UK. pp. 37–101.

[31] Goda, Y., 2000. Random Seas and Design of Maritime Structures, 2nd ed. World Scientific Publishing Company: Singapore. pp. 12–44.

[32] Nakajima, T., Saito, Y., Umeyama, M., 2022. A study on stability of floating architecture and its design methodology. Proceedings of the Second World Conference on Floating Solutions, Rotterdam; October 27–29, 2020; Rotterdam, Netherlands (Rotterdam, NL). pp. 273–296.

[33] Xu, H., Neng, P., Yang, F., 2019. Motion response analysis of mining vessel based on ANSYS/AQWA. Journal of Physics: Conference Series. 1300(1), 012010.

[34] Wang, G., Goldfeld, Y., Drimer, N., 2019. Expanding coastal cities - Proof of feasibility for modular floating structures (MFS). Journal of Cleaner Production. 222, 520–538.

[35] Wang, G., Drimer, N., Goldfeld, Y., 2020. Modular floating structures (MFS) for offshore dwelling a hydrodynamic analysis in the frequency domain. Ocean Engineering. 216, 107996.

[36] Chakrabarti, S., 2001. Empirical calculation of roll damping for ships and barges. Ocean Engineering. 28(7), 915-932.

[37] ISO 10137:2007. 2007. Bases for design of structures - Serviceability of buildings and walkways against vibrations.

[38] Boggs, D., 1997. Acceleration Indexes for Human Comfort in Tall Buildings - Peak or RMS?. Council on Tall Buildings and Urban Habitat Monograph. 13, 1–21.